https://www.scirp.org/journal/ns Natural Science, 2022, Vol. 14, (No. 3), pp: 133-147

Effect of the Instrument Slit Function on Upwelling Radiance from a Wavelength Dependent Surface Reflectance

Rajinder K. Jagpal[1,2], Rehan Siddiqui[1,2,3], Sanjar M. Abrarov[1,3,4], Brendan M. Quine[2,3,4]

[1]Epic College of Technology, Mississauga, Canada; [2]Department of Physics and Astronomy, York University, Toronto, Canada; [3]Department of Earth and Space Science and Engineering, York University, Toronto, Canada; [4]Thoth Technology Inc., Algonquin Radio Observatory, Pembroke, Canada

Correspondence to: Rehan Siddiqui, rehan@epiccollege.ca

Keywords: Radiance Enhancement, Upwelling Radiance, Line-by-Line Computation, Radiative Transfer Model

Received: January 20, 2022 **Accepted:** March 26, 2022 **Published:** March 29, 2022

ABSTRACT

The Radiance Enhancement (RE) method was introduced for efficient detection of clouds from the space. Recently, we have also reported that due to high reflectance of combustion-originated smokes, this approach can also be generalized for detection of the forest fires by retrieving and analyzing datasets collected from a space orbiting micro-spectrometer operating in the near infrared spectral range. In our previous publication, we have performed a comparison of observed and synthetic radiance spectra by developing a method for computation of surface reflectance consisting of different canopies by weighted sum based on their areal coverage. However, this approach should be justified by a method based on corresponding proportions of the upwelling radiance. The results of computations we performed in this study reveal a good match between areal coverage of canopies and the corresponding proportions of the upwelling radiance due to effect of the instrument slit function.

1. INTRODUCTION

The detection of the upwelling radiance (also known as the flux) from space, especially in the near infrared (NIR) spectral regions, plays an important role in Atmospheric Science. In particular, this technique provides data that can be used to retrieve valuable information about atmospheric constituents of the gases and condition of the surface. The large-scale datasets collected from space by a micro-spectrometer orbiting around the Earth can be retrieved to obtain the mixing ratios of the atmospheric gases like CO_2, CO, H_2O, CH_4, O_2, O_3, N_2O [1-6] and to estimate levels of particulate matter, especially hazardous $PM_{2.5}$ particles [7]. This type of large-scale remote space data is used by our research group to detect and monitor the sources of some greenhouse gases [5, 6, 8-10]. The retrieved results of the NIR space data can be

used not only to analyze and trace greenhouse gases, but also to predict their tendency and dynamics.

We have shown recently that the datasets of the upwelling radiance collected from a space remote sensor can also be used for efficient detection of cloud scenes by using the Radiance Enhancement method [11-14]. Specifically, the RE method utilizes the line-by-line radiative transfer model GENSPECT [15] in order to match the synthetic radiance with observed radiance by incrementing or decrementing several variables like concentration of gases, zenith angle, deviation of the nadir angle, etc. The computation is performed in a nested loop until a best match of synthetic and observed radiance spectra is achieved. A least square method is applied as a criterion to match the computed and observed data [14]. Apart from the variable parameters, the wavelength dependency of the reflecting surface has to be taken into consideration.

The RE method is based on the following two formulas [11-14]

$$RE_i = \frac{1}{N}\sum_{j=1}^{J}\left\{\frac{OBS_i[j]-SYN_i[j]}{SYN_i[j]}\right\},$$

and

$$CRE_i = \sum_{i=1}^{N} RE_i,$$

where i is the index of wavelength sub-bands, j is the index of grid-points, J is the total number of the grid-points and N is the number of sub-bands that can be taken as 4. The first formula signifies RE associated with sub-band i while the second formula defines the combined radiance enhancement (CRE) for all considered sub-bands.

The RE method utilizes datasets obtained from the ultra-light and small-size space-orbiting Argus 1000 micro-spectrometer that was launched into space from India in 2008 [6] as a payload of the CanX-2 nano-satellite [16]. This space instrument operates in the NIR range from 1100 nm to 1700 nm with spatial resolution on the ground about 1400 × 1100 m^2 [6]. By computing frequency of events as a function of the CRE, one can estimate the chances for observation of the cloud scenes. The detailed description of the RE method is described in the work [11].

Since the RE method utilizes the Argus datasets, it is developed to cover the wide NIR range from 1100 nm to 1700 nm. Therefore, due to wide spectral range, it takes into the consideration the wavelength dependency of the surface reflectance. However, if the Earth surface is not homogeneous, then the cumulative effect of upwelling radiance from each surface component must be considered. The landscapes over Canada include prairies, forests, lakes, rivers and mixed lands. The prairies are predominantly covered with grass and soil while the forests are covered with pine trees, broadleaf trees and bushes. There are vast mixed lands in North America that may include each component in different proportions [17, 18].

In order to resolve the problem of surface albedo inhomogeneity, we applied a method based on areal coverage of each specific canopy [14]. However, this method has not been correlated with corresponding proportions of the upwelling radiance contributed by each type of canopy from the ground. Therefore, the computations we performed in the retrieval in our recent work [14] should be rigorously justified by this correlation. In this work, we show the numerical evidence that fully justifies approach based on areal coverage [14]. In particular, the numerical analysis we performed reveals that the instrument slit function plays a key role in such a correlation between methods based on areal coverage and corresponding proportions of the upwelling radiance.

2. RESULTS AND DISCUSSION

2.1. Motivation

Since field of view of the Argus 1000 instrument covers the area about 1.56 km^2 [6], it is very likely to expect that the upwelling radiance originates from inhomogeneous surface albedo. In general, therefore,

the upwelling radiance is supposed to be due to combined radiances from different canopies. Considering nadir view [6], we may expect that the soil, pine trees, vegetation (broadleaf trees and bushes) and grass may be the major contributors for the reflectance.

Figure 1 shows reflectance as a function of the wavelength for the soil, pine trees, vegetation and grass. The data for reflectance spectra can be gathered from the following spectral data sources [19-22]. We can consider, for example, the areal coverage beneath field of view of Argus instrument for these canopies to be 13.33%, 20%, 40% and 26.67%, respectively. This is a typical observation for subarctic zones of Canada.

The chill weather and clean environment are very vital factors for successful reproduction and growth of the pine trees [23]. However, due to increasing atmospheric temperature appearing as a result of rapid increase of the CO_2 greenhouse gas over last decades [24, 25], increased level of industrial pollutants [26] and wildfires [27-29], the broadleaf plants competing with pine trees have more chances to progressively replace them. Pine trees provide the most valuable wood in construction industry. Therefore, these trees are logged in a commercially colossal scale for internal and worldwide trade. Pine trees are very slow in growth and, unlike many other species. They need several decades for recovery. As a result, we can see a significant domination of the broadleaf plants especially near the farms and villages in the rural areas of Canada. As a consequence, the areal coverage proportion of broadleaf trees and bushes to pine trees becomes larger year by year and in many places like the Wood Buffalo National Park of Canada and Algonquin National Park of Canada. Unfortunately, such a tendency becomes normal even at Northern Subarctic of Canada, where cold weather and clean environmental conditions were considered ideal for growth of the pine trees in the recent past [23]. As the increase of broadleaf plants appearing as a result of increasing atmospheric temperature is a current issue, we may attempt to analyze how the reflectance may change as a result of the increasing contribution of the vegetation. Considering that the relative areal coverage proportions of the soil, pine trees and grass remains same and increasing the contribution of the vegetation from 0 to 1, we can compute the reflectance as a function of the contribution factor of vegetation.

The results of computation in illustrated in the **Figure 2** showing how the increase of vegetation affects the cumulative reflectance. Inset in **Figure 2** shows the Wood Buffalo National Park of Canada, obtained from Google Map [30]. As we can see, the surface albedo is not uniform and mostly consists of soil,

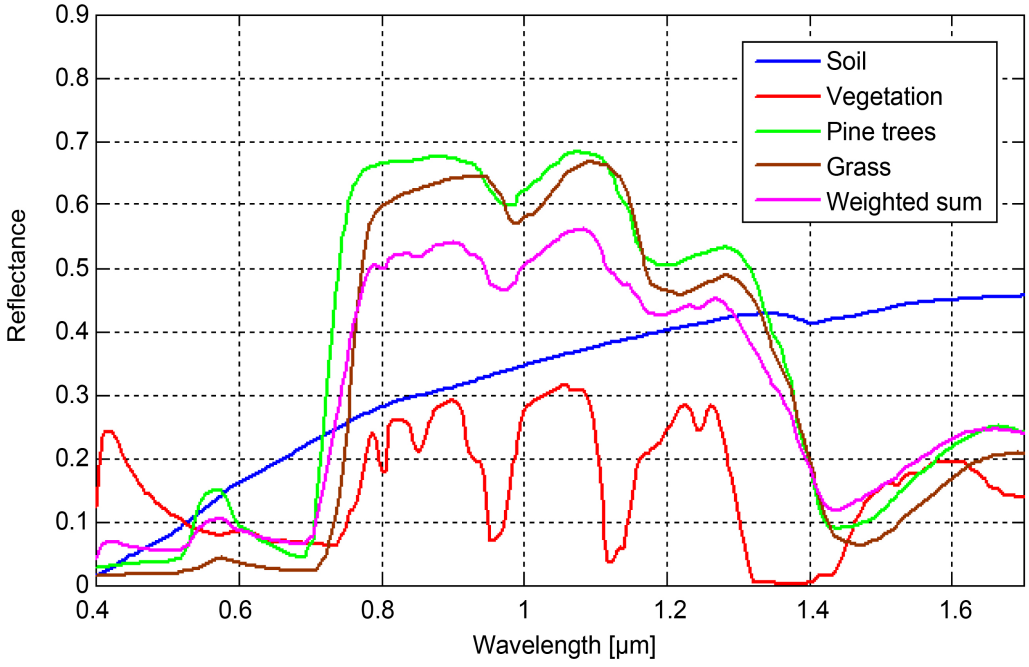

Figure 1. Wavelength dependent reflectance for different surfaces [19-22].

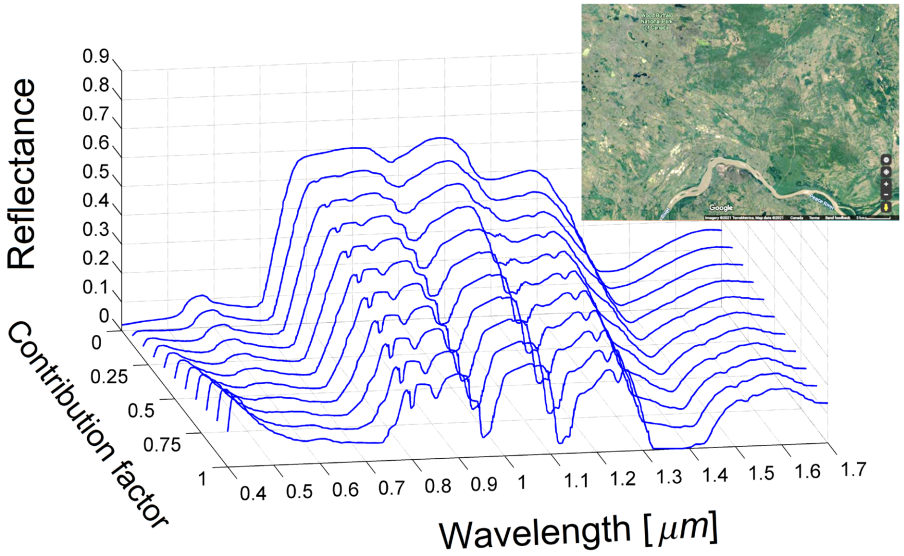

Figure 2. Evolution of the reflectance as a function of the contribution factor. Inset shows a typical landscape area over the Wood Buffalo National Park of Canada obtained from Google Map [30].

pine trees, vegetation and grass. The areal coverage by different canopies can be estimated from the Google image taken over the local terrain. By taking the areal coverage proportions, say, as 13.33%, 20%, 40% and 26.67%, respectively, we can compute the cumulative radiance by weighted sum. This signifies that parts of instrument's field of view 1.56 km^2 occupied by soil, pine trees, vegetation and grass are 0.1333, 0.2, 0.4 and 0.2667, respectively. The curve of cumulative reflectance obtained by weighted sum can be seen in **Figure 1**, shown by magenta color.

In order to simulate the upwelling radiance we applied the most recent version that accounts for the multiple scattering schemes in the line-by-line (LBL) radiative transfer model GENSPECT [15] with the HITRAN molecular spectroscopic database [31]. In the updated version we applied a single domain interpolation of the Voigt function [32] in which any of our three algorithms [33, 34] or [35] can be implemented to generate highly accurate references. This new method accelerates the computation and, in contrast to traditional method of LBL computation, enables us to avoid unnecessary interpolation of the absorption coefficients [36, 37]. Furthermore, we developed some additional MATLAB library files in order to perform computation of the cumulative weighted sum within a wide spectral range.

In the simplest case we can take surface reflectance to be a constant. This is shown in the **Figure 3** by gray highly oscillated curve. However, such a simplification does not describe the real scenario when we deal with a very wide spectral range. In case of the wavelength dependency of the surface albedo, the shape of the relative positions of the spectral lines can significantly change. This effect of the wavelength dependency of reflectance can be seen from **Figure 3** for soil, pine trees, vegetation and grass by blue, red, green and brown highly oscillated curves, respectively.

Due to a limited resolution of any spectrometer the high-frequency oscillation in upwelling radiance cannot be observed. In order to account for this limitation of the instrument we took into consideration the instrument slit function. The effect of the instrument slit function [38-40] can be seen from the **Figure 4** showing the upwelling radiance for soil, pine trees, vegetation and grass by blue, red, green and brown curves, respectively. The gray curve in this figure shows the upwelling radiance at constant reflectance. It should be noted that the shapes of these curves somehow resemble the shapes of the reflectance curves shown in **Figure 1**. Therefore, we may suggest that the radiance data collected from space by micro-spectrometers like Argus 1000 can also be used to retrieve wavelength dependent reflectance spectra by calibration.

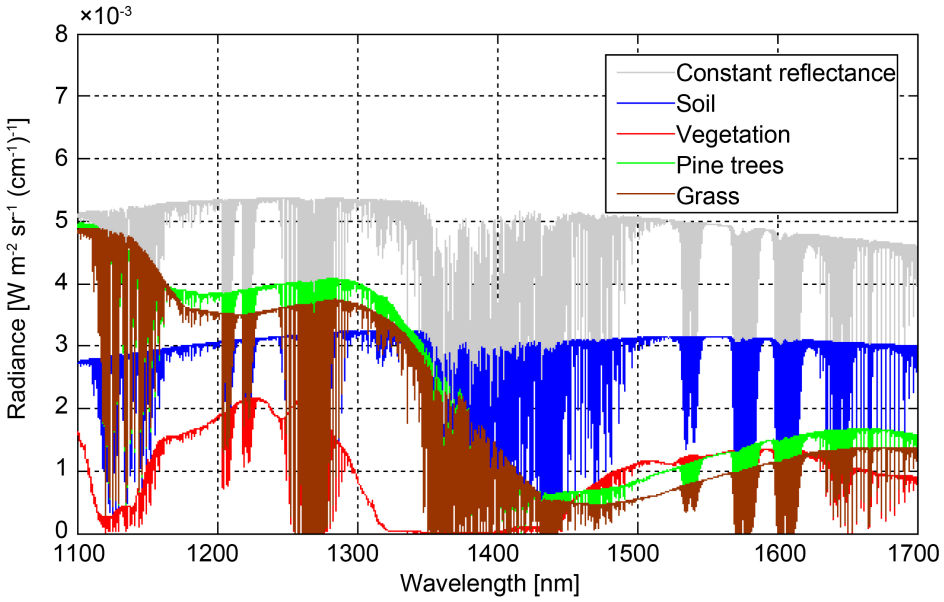

Figure 3. Synthetic radiance spectra upwelling from the different surfaces.

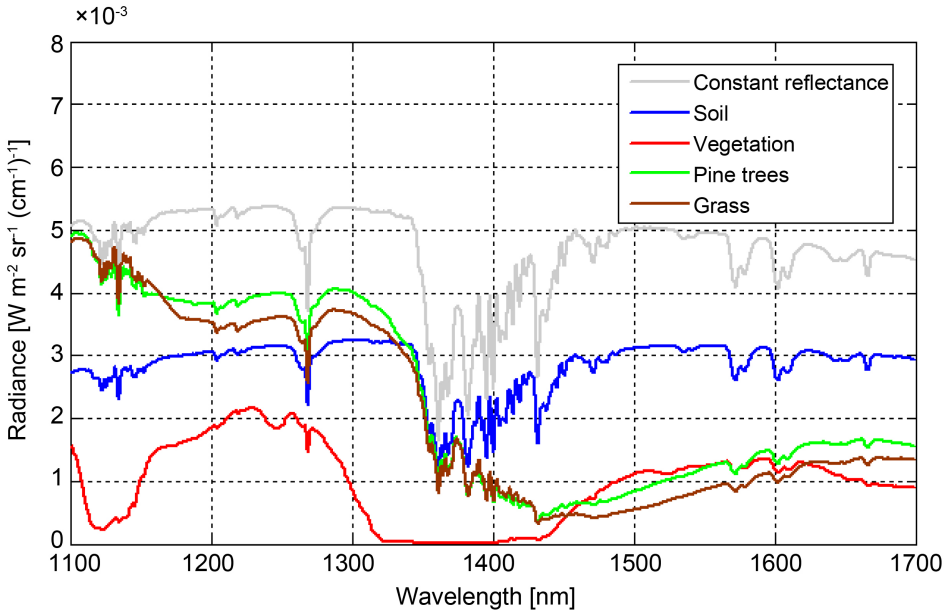

Figure 4. Synthetic radiance with instrument slit function for the different surfaces.

The Argus 1000 micro-spectrometer is designed to observe primarily CO_2 greenhouse gas. However, three other atmospheric gases H_2O, O_2 and CH_4 are also of the great interest. Such a choice of these particular four gases is due to their profound absorptions in the Argus remote sensor wavelength range 1100 nm to 1700 nm [6]. These absorption lines are most profound when the reflectance is a constant as shown in Figure 5. In particular, we can observe several sub-bands; relatively narrow sub-band near 1275 nm is due to O_2 molecules, wide sub-band starting from approximately 1350 nm to 1500 nm is due to water vapor H_2O, two close sub-bands near 1575 nm and 1600 nm are due to CO_2 and a narrow sub-band at 1675 nm is due to CH_4.

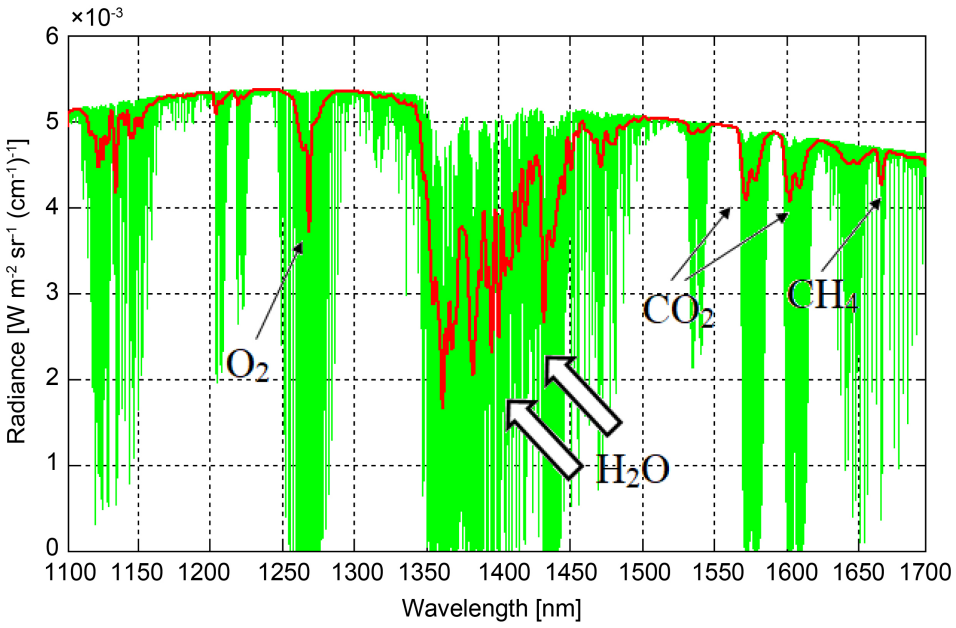

Figure 5. Synthetic radiance upwelling from a surface with wavelength independent reflectance.

The radiance $R(\nu, z_{obs})$, where ν is spatial frequency and z_{obs} is the observation point from space, can be defined as power per square meter per steradian per (spatial) frequency ($[\mathrm{Wm^{-2}\cdot sr^{-1}\cdot(cm^{-1})^{-1}}]$). The radiance upwelling from the Earth surface accounts for both, reflected and emitted radiance. The upwelling radiance from the surface canopies may occur as a result of photon absorption/re-emission and reflectance. In general, the computation of the radiance may be complicated due to inhomogeneity of atmospheric column. The inhomogeneity includes multiple scattering, pressure and temperature variations with height, mixing ratio of the gases and so on. One of the efficient ways to resolve this problem is to slice the atmospheric column into cells such that each cell can be regarded as pseudo-homogeneous. Although slicing atmospheric column into layers (or cells) makes the computation more intense, it resolves many complexities and provides more realistic and reliable results. The technical aspects in computation of the radiance by a LBL radiative transfer atmospheric model can be found elsewhere [41-45].

Our preference for the unit $[\mathrm{Wm^{-2}\cdot sr^{-1}\cdot(cm^{-1})^{-1}}]$ involving spatial frequency is due to classic work of Edwards [41], where an efficient LBL application for a radiative transfer model was developed and implemented. Furthermore, the similar units in energy-related parameters, expressed in terms of spatial frequency $\mathrm{cm^{-1}}$, remains common in many spectroscopic applications [45].

In our recent publication we performed computation of the upwelling radiance by using a method based on areal coverage [14]. However, strictly saying this method is rather heuristic and, therefore, requires computational error analysis to validate it. Specifically, this method should be matched with that of based on a corresponding upwelling radiance proportions.

2.2. Methodology of Computation

A method based on areal coverage takes area proportions of the soil, pine trees, vegetation and grass within field of view of the space instrument. Based on these results the cumulative wavelength dependent reflectance $r_c(\lambda)$ is computed as a weighted sum that for our specific case is given by a method based on areal coverage takes area proportions of the soil, pine trees, vegetation and grass within field of view of the space instrument. Based on these results the cumulative wavelength dependent reflectance $r_c(\lambda)$ is computed as a weighted sum that for our specific case is given by

$$r_c(\lambda) = \omega_1 r_s(\lambda) + \omega_2 r_{pt}(\lambda) + \omega_3 r_v(\lambda) + \omega_4 r_g(\lambda),$$

where $\omega_1 = 0.1333$, $\omega_2 = 0.2$, $\omega_3 = 0.4$ and $\omega_4 = 0.2667$ are weighted coefficients such that $\omega_1 + \omega_2 + \omega_3 + \omega_4 = 1$ while $r_s(\lambda)$, $r_{pt}(\lambda)$, $r_v(\lambda)$ and $r_g(\lambda)$ are reflectance of the soil, pine trees, vegetation and grass dependent on wavelength λ. Once the cumulative reflectance is found, the LBL computation can be performed for upwelling radiance. As we can see from Figure 1 reflectance functions from pine tree and grass resemble to each other. Therefore, we should not expect that their proportions would significantly affect the upwelling radiance. Also the reflectance curve of the soil is relatively flat within the range from 1100 nm to 1700 nm. That signifies that its contribution would also not affect much the shape of the upwelling radiance. However, the reflectance of the vegetation is significantly different; it is not flat and does not resemble any other curves. Consequently, the contribution factor from the vegetation may have the largest impact to the upwelling radiance.

A method based on upwelling radiance proportions is different. Instead of computing cumulative reflectance by using the areal coverage, it utilizes following weighted sum formula

$$R(\nu, z_{obs}) = \omega_1 R_s(\nu, z_{obs}) + \omega_2 R_{pt}(\nu, z_{obs}) + \omega_3 R_v(\nu, z_{obs}) + \omega_4 R_g(\nu, z_{obs}),$$

where $R_s(\nu, z_{obs})$, $R_{pt}(\nu, z_{obs})$, $R_v(\nu, z_{obs})$ and $R_g(\nu, z_{obs})$ are radiance functions due to contribution of soil, pine trees, vegetation and grass, respectively.

The first method of computation is more practical as it is easier to implement and it takes less amount of time for computation. The second method, however, is more rigorous as it accounts for the contribution of each component of the ground albedo. Ideally, when $r_s(\lambda)$, $r_{pt}(\lambda)$, $r_v(\lambda)$ and $r_g(\lambda)$ are wavelength independent, then both methods provide the same result. However, because of wavelength dependence of the surface albedo, one should expect some discrepancies in computation of the upwelling radiance and evaluate numerically whether or not these discrepancies are negligible.

Figure 6 shows synthetic radiance computed by areal coverage. The spectral radiance is due to solar light reflection from the surface covered by different canopies. Solar light in this spectral range is mostly reflected. However, a smallest portion of the solar light is absorbed and then reemitted by the surface canopies.

Figure 7 depicts synthetic radiance computed by corresponding upwelling radiance proportions for soil, pine trees, vegetation and grass canopies. At the first glance these two figures look very similar.

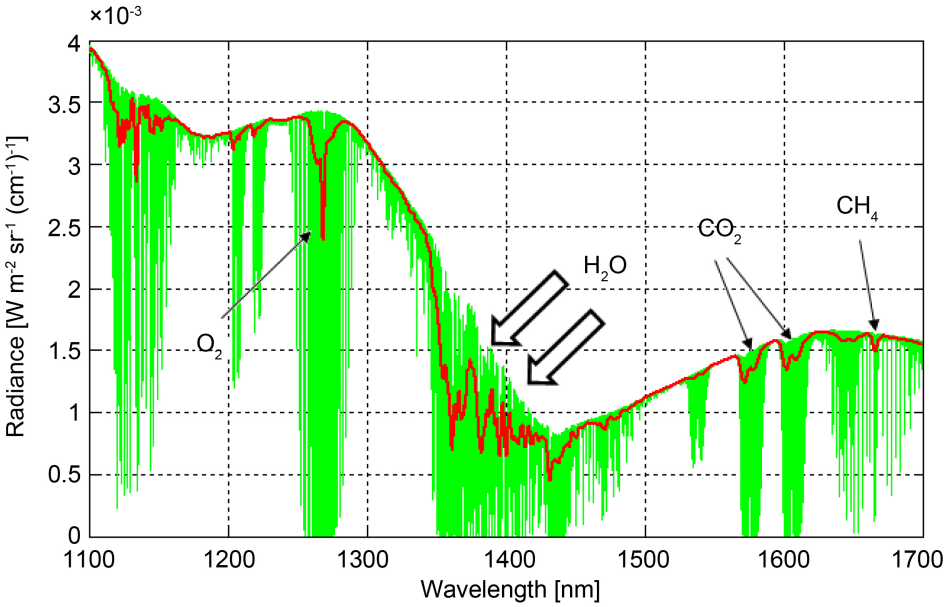

Figure 6. Radiance computed by using the areal coverage method.

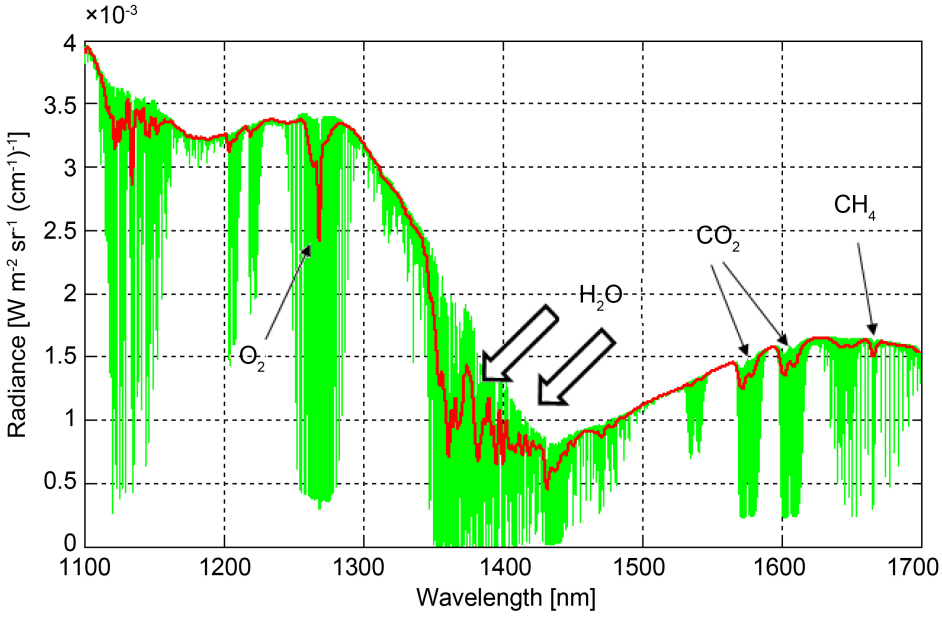

Figure 7. Radiance computed by using upwelling radiance proportions.

However, a more careful consideration reveals some discrepancies. In particular, once these two graphs from **Figure 6** and **Figure 7** are overlapped, we can notice the discrepancies near 1275 nm, 1575 nm and 1600 nm. This can be seen more clearly from the **Figure 8** illustrating synthetic radiance computed by areal coverage and by corresponding upwelling radiance proportions shown by magenta and blue colors.

Figure 9 shows absolute difference between these two methods. As we can see, the discrepancies are relatively large near 1275 nm, 1575 nm and 1600 nm. Consequently, one may assume that these two methods are not compatible at least near these three spectral locations. However, if we take into account the instrument slit function [38-40] then the results become absolutely different.

Consider **Figure 10** showing the synthetic radiance that accounts for the instrument slit function for these two methods. Visually there is no difference between curves. **Figure 11** shows the absolute difference between these two curves. As we can see from this figure, the absolute difference is smaller than the actual radiance by two orders of magnitude. This phenomenon can be explained from the fact that instrument slit function takes average of the highly oscillating synthetic radiance. The amplitude of oscillations may differ in these two methods. However, as an instrument slit function averages the highly oscillating synthetic radiance, both resultant curves become practically same along all wavelength range. Thus, we can see significance of the instrument slit function.

In order to verify applicability of these two methods for the entire range, we perform computation of the absolute difference as a function of contribution factor from vegetation. **Figure 12(a)** shows 3D plot of absolute difference and as we can see from this figure the worst case scenario occurs at lower frequencies and higher values of the contribution factor from vegetation. Overall, the absolute difference is by two orders of the magnitude lower (large blue area) than the smoothed upwelling radiance spectra shown in the **Figure 10**. However, as we can see from this **Figure 12(a)** even the largest absolute difference is by more than 10 times smaller. Furthermore, the red area with largest absolute difference is very narrow and negligibly small. This can be seen from **Figure 12(b)** at the top left corner showing upper view of the same plot.

Thus, the error analysis performed with the LBL radiative transfer model reveals that the method of computation based on areal coverage is completely justifiable. Both methods are equivalent for computation of the upwelling radiance. However, the method based on areal coverage is more practical. Such a good match between these two methods is due to effect of the instrument slit function that averages the

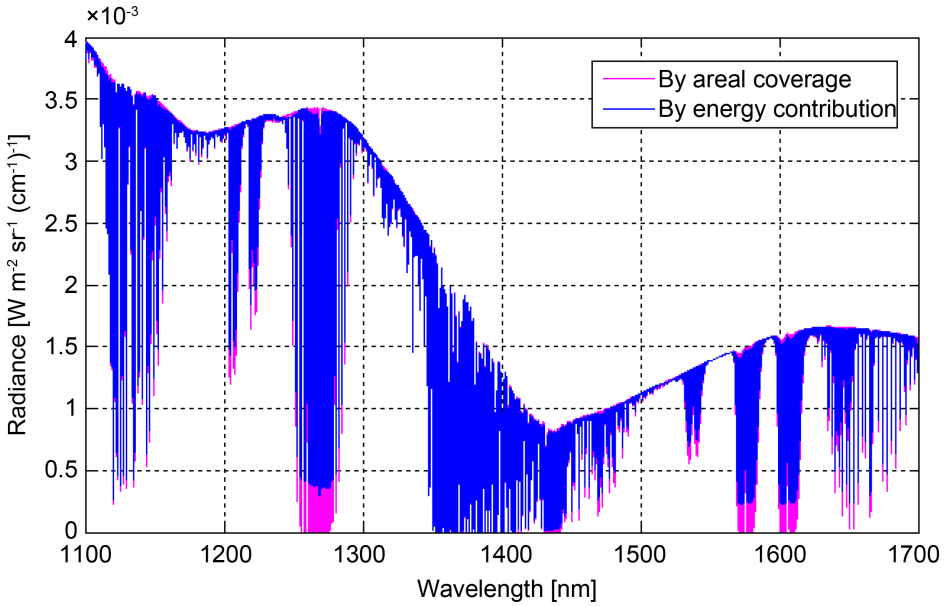

Figure 8. **Overlapped radiance spectra obtained by both methods of computation.**

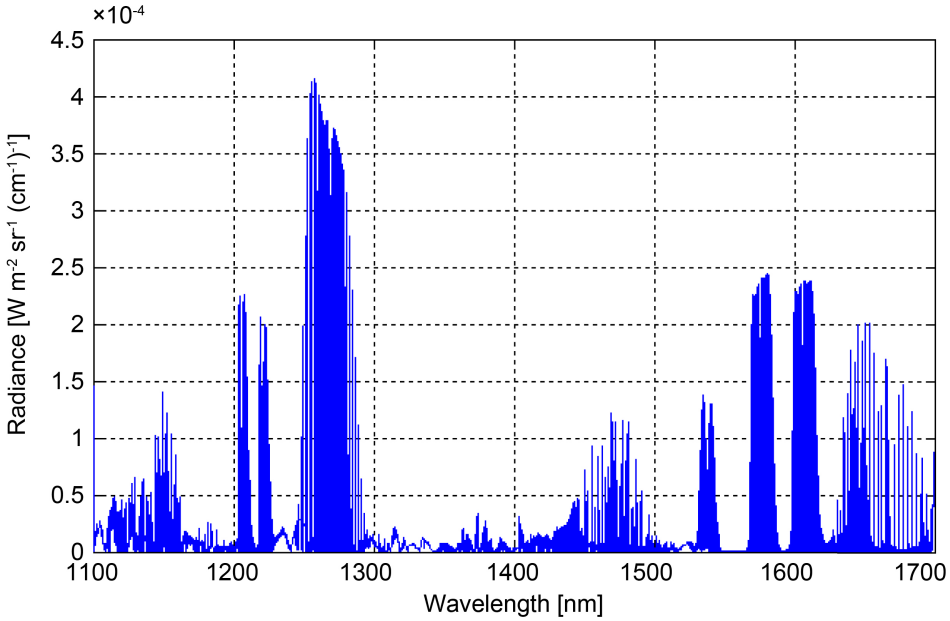

Figure 9. **Absolute difference of radiance spectra. Overlapped radiance spectra obtained by both methods of computation.**

highly oscillated synthetic radiance.

3. PIXEL WIDTH

The effect of the instrument slit function showing consistency of two weighted sum methods described above should also be verified numerically more generally. In particular, it is necessary to demonstrate that the effect of the slit function remains valid regardless the instrument resolution due to a weak

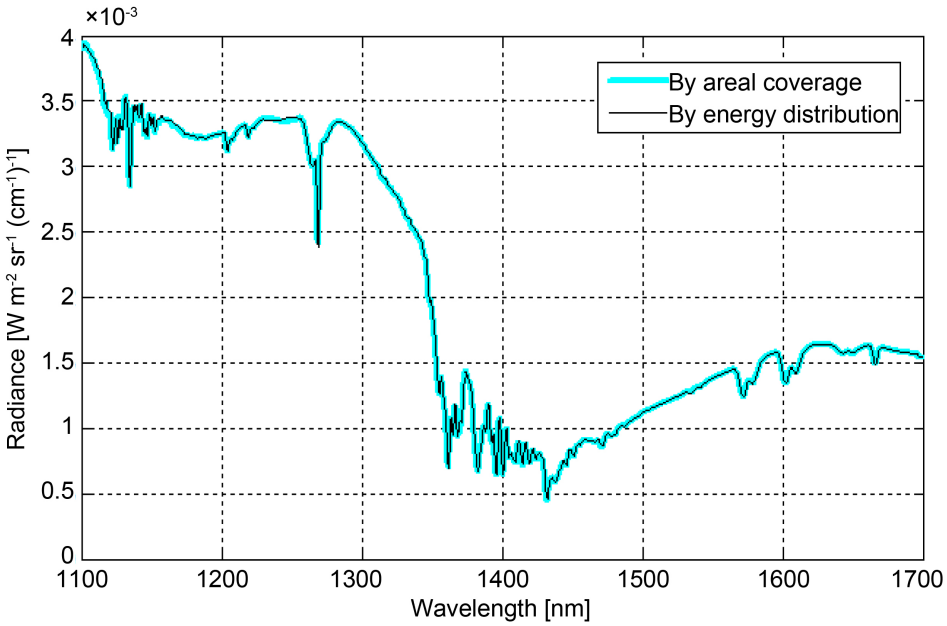

Figure 10. Smoothed radiance computed by both methods.

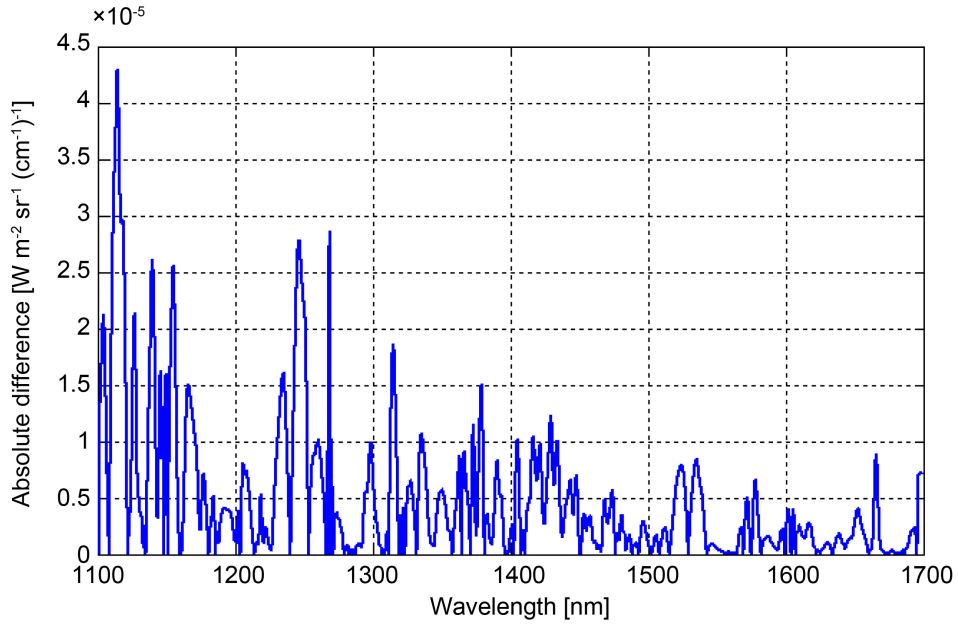

Figure 11. Absolute difference of radiance spectra with instrument slit function.

dependence of the absolute error between two weighted sum methods on pixel width of the micro-spectrometer.

The size and mass limitations of a micro-spectrometer are vital in launching instrument in space because of high-cost of a payload in nano-satellite. As a result of these limitations the resolution of a micro-spectrometer are not better than 1 nm. Typically, spectral resolution of a modern small-size and ultra-light micro-spectrometers like Argus 2000 for a space mission ranges between 1 nm to 10 nm [46]. A pixel width is an important parameter of a semiconductor array for detection of the light and one of the main

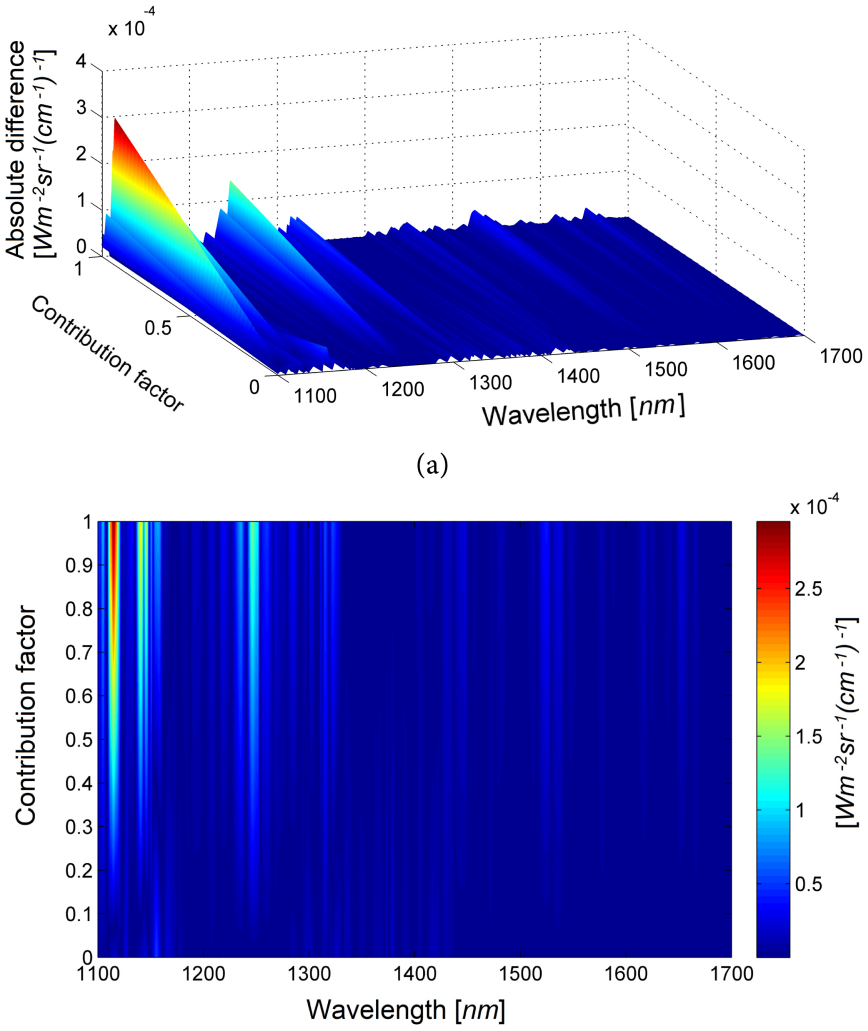

Figure 12. Absolute difference of radiance spectra with instrument slit function: (a) side view and (b) upper view.

factors that determines the spectral resolution of micro-spectrometer. Specifically, design of Argus micro-spectrometers include extended InGaAs semiconductor array consisting of more than 100 pixels in a configuration where each single pixel corresponds to the spectral counts at a particular wavenumber [6]. Therefore, the smaller pixel width implies a higher spectral resolution of the Argus space instrument.

Figure 13 shows a set of plots of absolute errors between two weighted sum methods at pixel widths 1 cm^{-1}, 5 cm^{-1}, 9 cm^{-1}, 13 cm^{-1}, 17 cm^{-1}, 21 cm^{-1} and 25 cm^{-1} by black, blue, red, green, brown, magenta and gray colors, respectively.

The pixel width range between 1 cm^{-1} to 25 cm^{-1} approximately corresponds to the spectral resolution range 0.2 nm to 6 nm. The highest point of the black curve corresponding to the pixel width 1 cm^{-1} is 4.99 $\times 10^{-5}$ $Wm^{-2}\cdot sr^{-1}\cdot(cm^{-1})^{-1}$ while the highest point of the gray curve corresponding to pixel width 25 cm^{-1} is 3.25 $\times 10^{-5}$ $Wm^{-2}\cdot sr^{-1}\cdot(cm^{-1})^{-1}$. Thus, we can see that the decrease of pixel width by factor 25 decreases absolute difference by factor $(4.99 \times 10^{-5})/(3.25 \times 10^{-5}) \approx 1.54$ only. Therefore, our numerical results confirm a weak dependence of the absolute error on the resolution of the instrument. This signifies that two weighted sum methods retain consistency even at a relatively high spectral resolution 0.2 nm of the remote sensor in detection of the light in the NIR spectral region 1100 nm to 1700 nm.

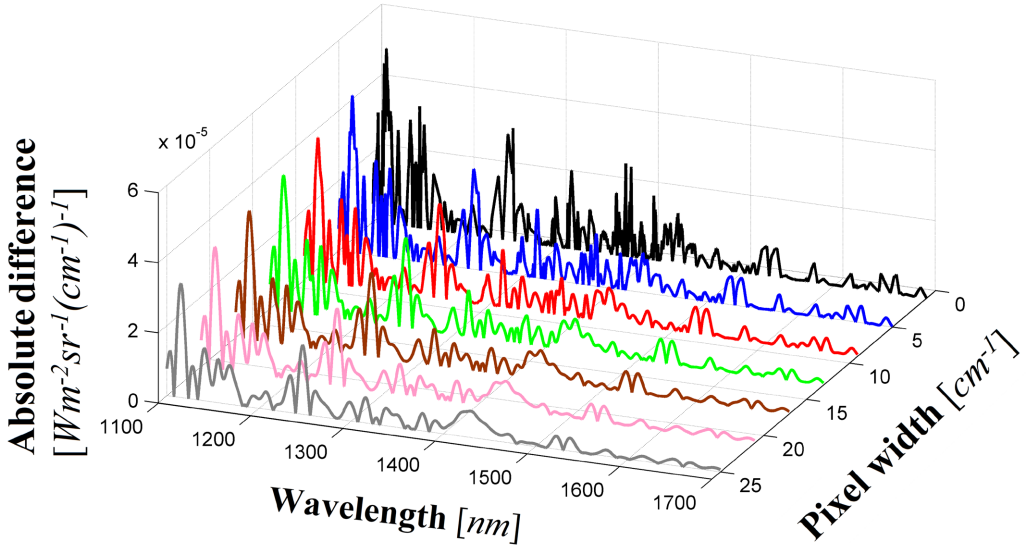

Figure 13. Absolute difference of radiance spectra at 1 cm^{-1}, 5 cm^{-1}, 9 cm^{-1}, 13 cm^{-1}, 17 cm^{-1}, 21 cm^{-1} and 25 cm^{-1} pixel widths shown by black, blue, red, green, brown, magenta and gray colors, respectively.

4. CONCLUSION

The RE method for efficient detection of clouds and forest fires from the space applies LBL radiative transfer code for computation of the upwelling radiance that accounts for the wavelength dependency of the surface albedo [14]. In particular, computation of the cumulative reflectance was based on areal coverage from each canopy. This method applies less computation since the second method based on corresponding radiance proportions requires separate computation for each canopy. Although the method of computation of the upwelling radiance based on areal coverage is more convenient in implementation, it should be validated by comparing it with method based on corresponding radiance proportions. The error analysis we performed shows that both methods are in good agreement with each other and, therefore, are virtually equivalent. In particular, our model shows that due to instrument slit function, the discrepancy between two methods near 1275 nm, 1575 nm and 1600 nm is by two orders of the magnitude smaller than the upwelling radiance. The good match between these two methods is due to instrument slit function that averages the highly oscillated upwelling radiance spectra. The proposed method can be used for retrieving space data from a micro-spectrometer operating in a NIR region. Numerical analysis we performed shows that two weighted sum methods retain consistency even at a relatively high spectral resolution 0.2 nm.

ACKNOWLEDGEMENTS

This study is supported by Department of Physics and Astronomy at York University, Department of Earth and Space Science and Engineering at York University, Thoth Technologies Inc., Epic College of Technology and Epic Climate Green (ECG) Inc.

CONFLICTS OF INTEREST

The authors declare no conflicts of interest regarding the publication of this paper.

REFERENCES

1. Buchwitz, M., Rozanov, V.V. and Burrows, J.P. (2000) A Near-Infrared Optimized DOAS Method for the Fast

Global Retrieval of Atmospheric CH_4, CO, CO_2, H_2O, and N_2O Total Column Amounts from SCIAMACHY Envisat-1 Nadir Radiances. *Journal of Geophysical Research*, **105**, 15231-15245. https://doi.org/10.1029/2000JD900191

2. Buchwitz, M., de Beek, R., Burrows, J.P., Bovensmann, H., Warneke, T., Notholt, J., Meirink, J.F., Goede, A.P.H., Bergamaschi, P., Körner, S., Heimann M. and Schulz, A. (2005) Atmospheric Methane and Carbon Dioxide from SCIAMACHY Satellite Data: Initial Comparison with Chemistry and Transport Models. *Atmospheric Chemistry and Physics*, **5**, 941-962. https://doi.org/10.5194/acp-5-941-2005
3. Buchwitz, M., de Beek, R., Noel, S., Burrows, J.P., Bovensmann, H., Bremer, H., Bergamaschi, P., Körner S. and Heimann, M. (2005) Carbon Monoxide, Methane and Carbon Dioxide Columns Retrieved from SCIAMACHY by WFM-DOAS: Year 2003 Initial Data Set. *Atmospheric Chemistry and Physics*, **5**, 3313-3329. https://doi.org/10.5194/acp-5-3313-2005
4. Bösch, H., Toon, G.C., Sen, B., Washenfelder, R.A., Wennberg, P.O., Buchwitz, M., de Beek, R., Burrows, J.P., Crisp, D., Christi, M., Connor, B.J., Natraj, V. and Yung, Y.L. (2006) Space-Based Near-Infrared CO_2 Measurements: Testing the Orbiting Carbon Observatory Retrieval Algorithm and Validation Concept Using SCIAMACHY Observations over Park Falls, Wisconsin. *Journal of Geophysical Research*, **111**, D23302. https://doi.org/10.1029/2006JD007080
5. Jagpal, R.K., Quine, B.M., Chesser, H., Abrarov S. and Lee, R. (2010) Calibration and In-Orbit Performance of the Argus 1000 Spectrometer—The Canadian Pollution Monitor. *Journal of Applied Remote Sensing*, **4**, Article ID: 049501. https://doi.org/10.1117/1.3302405
6. Jagpal, R.K. (2011) Calibration and Validation of Argus 1000 Spectrometer—A Canadian Pollution Monitor. PhD Thesis, York University, Toronto. https://doi.org/10.1117/1.3302405
7. Christopher S.A. and Gupta, P. (2010) Satellite Remote Sensing of Particulate Matter Air Quality: The Cloud-Cover Problem. *Journal of the Air & Waste Management Association*, **40**, 5880-5892. https://doi.org/10.3155/1047-3289.60.5.596
8. Jagpal, R.K., Siddiqui, R., Abrarov, S.M. and Quine, B.M. (2019) Carbon Dioxide Retrieval of Argus 1000 Space Data by Using GENSPECT Line-by-Line Radiative Transfer Model. *Environment and Natural Resources Research*, **9**, 77-85. https://doi.org/10.5539/enrr.v9n3p77
9. Siddiqui, R., Jagpal, J., Salem, N.A. and Quine, B.M. (2015) Classification of Cloud Scenes by Argus Spectral Data. *International Journal of Space Science and Engineering*, **3**, 295-311. https://doi.org/10.1504/IJSPACESE.2015.075911
10. Siddiqui, R., Jagpal, R.K. and Quine, B.M. (2017) Short Wave Upwelling Radiative Flux (SWupRF) within Near Infrared (NIR) Wavelength Bands of O_2, H_2O, CO_2 and CH_4 by Argus 1000 Along with GENSPECT Line-Byline Radiative Transfer Model. *Canadian Journal of Remote Sensing*, **43**, 330-344. https://doi.org/10.1080/07038992.2017.1346467
11. Siddiqui, R. (2017) Efficient Detection of Cloud Scenes by a Space-Orbiting Argus 1000 Micro-Spectrometer. PhD Thesis, York University, Toronto.
12. Siddiqui, R., Jagpal, R.K. and Abrarov, S.M. and Quine, B.M. (2020) Radiance Enhancement and Shortwave Upwelling Radiative Flux Methods for Efficient Detection of Cloud Scenes. *International Journal of Space Science and Engineering*, **6**, 1-27. https://doi.org/10.1504/IJSPACESE.2020.109745
13. Siddiqui, R. and Jagpal, R.K., Abrarov, S.M. and Quine, B.M. (2020) A New Approach to Detect Combustion-Originated Aerosols by Using a Cloud Method. *AGU Fall Meeting* 2020, 1-17 December 2020.
14. Siddiqui, R., Jagpal, R.K., Abrarov, S.M. and Quine, B.M. (2021) Efficient Application of the Radiance Enhancement Method for Detection of the Forest Fires due to Combustion-Originated Reflectance. *Journal of Environmental Protection*, **12**, 717-733. https://doi.org/10.4236/jep.2021.1210043

15. Quine, B.M. and Drummond, J.R. (2002) GENSPECT: A Line-by-Line Code with Selectable Interpolation Error Tolerance. *Journal of Quantitative Spectroscopy & Radiative Transfer*, **74**, 147-165. https://doi.org/10.1016/S0022-4073(01)00193-5

16. Rankin, D., Kekez, D.D., Zee, R.E., Pranajaya, F.M., Foisy D.G. and Beattie, A.M. (2005) The CanX-2 Nanosatellite: Expanding the Science Abilities of Nanosatellites. *Acta Astronautica*, **57**, 167-174. https://doi.org/10.1016/j.actaastro.2005.03.032

17. Toot, R., Frelich, L.E., Butler, E.E. and Peter, B. (2020) Reich Climate-Biome Envelope Shifts Create Enormous Challenges and Novel Opportunities for Conservation. *Forests*, **11**, 1015. https://doi.org/10.3390/f11091015

18. Anderson, R.C. (2006) Evolution and Origin of the Central Grassland of North America: Climate, Fire, and Mammalian Grazers. *The Journal of the Torrey Botanical Society*, **133**, 626-647. https://doi.org/10.3159/1095-5674(2006)133[626:EAOOTC]2.0.CO;2

19. Roberts, Y.L., Pilewskie, P., Kindel, B.C., Feldman, D.R. and Collins, W.D. (2013) Quantitative Comparison of the Variability in Observed and Simulated Shortwave Reflectance. *Atmospheric Chemistry and Physics*, **13**, 3133-3147. https://doi.org/10.5194/acp-13-3133-2013

20. Li, S., Suna, D., Goldberg, M.D., Sjoberg, B., Santek, D., Hoffman, J.P., DeWeese, M., Restrepo, P., Lindsey, S. and Holloway, E. (2018) Automatic near Realtime Flood Detection Using Suomi-NPP/VIIRS Data. *Remote Sensing of Environment*, **204**, 672-689. https://doi.org/10.1016/j.rse.2017.09.032

21. MODIS Land. https://modis-land.gsfc.nasa.gov

22. Baldridge, A.M., Hook, S.J., Grove, C.I. and Rivera, R. (2009) The ASTER Spectral Library Version 2.0. *Remote Sensing of Environment*, **113**, 711-715. https://doi.org/10.1016/j.rse.2008.11.007

23. Dick, M., Porter, T.J., Pisaric, M.F.J., Wertheimer, È., de Montigny, P., Perreault, J.T. and Robillard, K.-L. (2014) A Multi-Century Eastern White Pine Tree-Ring Chronology Developed from Salvaged River Logs and Its Utility for Dating Heritage Structures in Canada's National Capital Region. *Dendrochronologia*, **32**, 120-126. https://doi.org/10.1016/j.dendro.2014.02.001

24. Apadula, F., Cassardo, C., Ferrarese, S., Heltai, D. and Lanza, A. (2019) Thirty Years of Atmospheric CO_2 Observations at the Plateau Rosa Station, Italy. *Atmosphere*, **10**, 418. https://doi.org/10.3390/atmos10070418

25. Karnauskas, K.B., Miller, S.L. and Schapiro, A.C. (2020) Fossil Fuel Combustion Is Driving Indoor CO_2 toward Levels Harmful to Human Cognition. *Geo-Health*, **4**, e2019GH000237. https://doi.org/10.1029/2019GH000237

26. Davidson, C.J., Foster, K.R. and Tanna, R.N. (2020) Forest Health Effects Due to Atmospheric Deposition: Findings from Long-Term Forest Health Monitoring in the Athabasca Oil Sands Region. *Science of the Total Environment*, **699**, Article ID: 134277. https://doi.org/10.1016/j.scitotenv.2019.134277

27. Tymstra, C., Stocks, B.J., Cai, X. and Flannigan, M.D. (2020) Wildfire Management in Canada: Review, Challenges and Opportunities. *Progress in Disaster Science*, **5**, Article ID: 100045. https://doi.org/10.1016/j.pdisas.2019.100045

28. Axelson, J.N., Alfaro, R.I. and Hawkes, B.C. (2009) Influence of Fire and Mountain Pine Beetle on the Dynamics of Lodgepole Pine Stands in British Columbia, Canada. *Forest Ecology and Management*, **257**, 1874-1882. https://doi.org/10.1016/j.foreco.2009.01.047

29. Benali, A., Russo, A., Sà, A.C.L., Pinto, R.M.S., Price, O., Koutsias, N. and Pereira, J.M.C. (2016) Determining Fire Dates and Locating Ignition Points with Satellite Data. *Remote Sensing*, **8**, 326. https://doi.org/10.3390/rs8040326

30. Google Earth. https://www.google.com/earth

31. Hill, C., Gordon, I.E., Kochanov, R.V., Barrett, L., Wilzewski, J.S. and Rothman, L.S. (2016) HITRANonline: An Online Interface and the Flexible Representation of Spectroscopic Data in the HITRAN Database. *Journal of Quantitative Spectroscopy & Radiative Transfer*, **177**, 4-14. https://doi.org/10.1016/j.jqsrt.2015.12.012

32. Abrarov, S.M., Quine, B.M., Siddiqui, R. and Jagpal, R.K. (2019) A Single-Domain Implementation of the Voigt/Complex Error Function by Vectorized Interpolation. *Earth Science Research*, **8**, 52-63. https://doi.org/10.5539/esr.v8n2p52

33. Abrarov, S.M. and Quine, B.M. (2011) Efficient Algorithmic Implementation of the Voigt/Complex Error Function Based on Exponential Series Approximation. *Applied Mathematics and Computation*, **218**, 1894-1902. https://doi.org/10.1016/j.amc.2011.06.072

34. Abrarov, S.M., Quine, B.M. and Jagpal, R.K. (2018) A Sampling-Based Approximation of the Complex Error Function and Its Implementation without Poles. *Applied Numerical Mathematics*, **129**, 181-191. https://doi.org/10.1016/j.apnum.2018.03.009

35. Abrarov, S.M. and Quine, B.M. (2018) A Rational Approximation of the Dawson's Integral for Efficient Computation of the Complex Error Function. *Applied Mathematics and Computation*, **321**, 526-543. https://doi.org/10.1016/j.amc.2017.10.032

36. Fomin, B.A. (1995) Effective Interpolation Technique for Line-by-Line Calculations of Radiation Absorption in Gases. *Journal of Quantitative Spectroscopy & Radiative Transfer*, **53**, 663-669. https://doi.org/10.1016/0022-4073(95)00029-K

37. Sparks, L. (1997) Efficient Line-by-Line Calculation of Absorption Coefficients to High Numerical Accuracy. *Journal of Quantitative Spectroscopy & Radiative Transfer*, **57**, 631-650. https://doi.org/10.1016/S0022-4073(96)00154-9

38. Beirle, S., Lampel, J., Lerot, C., Sihler, H. and Wagner, T. (2017) Parameterizing the Instrumental Spectral Response Function and Its Changes by a Super-Gaussian and Its Derivatives. *Atmospheric Measurement Techniques*, **10**, 581-598. https://doi.org/10.5194/amt-10-581-2017

39. Galan, L.D. and Winefordner, J.D. (1968) Slit Function Effects in Atomic Spectroscopy. *Spectrochemica Acta B*, **23**, 277-289. https://doi.org/10.1016/0584-8547(68)80007-2

40. Röseler, A. (1966) Measurements of the Instrument Function and of the Spectral Slit width of a Prism Spectrometer. *Infrared Physics*, **6**, 111-122. https://doi.org/10.1016/0020-0891(66)90005-4

41. Edwards, D.P. (1992) GENLN2: A General Line-by-Line Atmospheric Transmittance and Radiance Model, Version 3.0 Description and Users Guide. NCAR/TN-367-STR, National Center for Atmospheric Research, Boulder.

42. Liou, K.N. (2002) An Introduction to Atmospheric Radiation. 2nd Edition, Academic Press, Cambridge.

43. Edwards, D.P. (1987) GENLN2: The New Oxford Line-by-Line Atmospheric Transmission/Radiance Model. Dept. of Atmospheric, Oceanic and Planetary Physics, Memorandum 87.2, University of Oxford, Oxford.

44. Edwards, D.P. (1988) Atmospheric Transmittance and Radiance Calculations Using Line-by-Line Computer Models. *Proceedings*, *Modeling of the Atmosphere*, 1988 *Technical Symposium on Optics*, *Electro-Optics*, *and Sensors*, Orlando, Volume 928, 94-116. https://doi.org/10.1117/12.975622

45. Nordebo, S. (2021) Uniform Error Bounds for Fast Calculation of Approximate Voigt Profiles. *Journal of Quantitative Spectroscopy & Radiative Transfer*, **270**, Article ID: 107715. https://doi.org/10.1016/j.jqsrt.2021.107715

46. Jallad, A.-H., Marpu, P., Aziz, Z.A., Marar, A.A. and Awad, M. (2019) MeznSat—A 3U Cubesat for Monitoring Greenhouse Gases Using Short Wave Infrared Spectrometry: Mission Concept and Analysis. *Aerospace*, **6**, 118. https://doi.org/10.3390/aerospace6110118